## RESEARCH ARTICLE

**Key Points:**

- Directly adding all contributions from spray droplets in bulk models may introduce overestimates on spray-mediated heat fluxes
- We improved the overestimation issue in bulk model for the total heat flux by considering the effects of spray time scales
- Using the volume-weighted mean size as a representative size could simplify the quantifying of air-sea fluxes in an Eulerian framework

**Correspondence to:**
D. Richter,
David.Richter.26@nd.edu

# Influences of Polydisperse Sea Spray Size Distributions on Model Predictions of Air-Sea Heat Fluxes

**Tianze Peng[1]** [iD] **and David Richter[1]** [iD]

[1]Department of Civil & Environmental Engineering and Earth Sciences, University of Notre Dame, Notre Dame, IN, USA

**Abstract** Quantifying the influence of sea spray on air-sea fluxes under high-wind conditions is challenging due to a variety of factors. Among existing models, the so-called bulk air-sea flux model is commonly used in meteorological applications due to its simplicity, which often involves strong but untested assumptions on spray-mediated heat fluxes and feedback effects. For example, a common assumption is to treat each droplet size as an independent contribution; that is, it does not interact with other sizes. Thus, the interactions between different size classes of spray are often neglected. In this study, we focus on the polydispersity of the spray size distribution and investigate the appropriateness of assuming an independent contribution from different spray size classes. We implement direct numerical simulations (DNS) with Lagrangian tracking of spray droplets. Based on DNS results, the bulk spray model fails to capture the interactions between different sizes that are observed directly from the droplet and feedback statistics in DNS. Thus, assuming independent contributions from spray droplets results in significant overestimates on the total heat fluxes. We further test different representative sizes of a spray size distribution. We find that the volume-weighted representative size is capable of predicting the droplet-modified temperature and humidity fields and generally captures the vertical profiles of spray-mediated and interfacial heat fluxes. The results indicate that the computation of spray-mediated fluxes can be simplified in large-scale parameterizations.

## 1. Introduction

The dynamic and thermodynamic effects of sea spray at the air-sea interface have been studied from a wide range of perspectives and methodologies. One primary interest is the quantification of spray's influence on the surface heat and moisture fluxes at the lower atmospheric boundary layer, in particular under high wind conditions, which is related to the formation and intensity of the tropical cyclones (Andreas & Emanuel, 2001; Bell et al., 2012; Emanuel, 1986, 2003; Gall et al., 2008; Richter & Stern, 2014; Schade & Emanuel, 1999). Recent studies also show the importance of spray effects on air-sea gas exchange (Andreas et al., 2016; Gonçalves & Innocentini, 2018; Monahan et al., 2017).

A complete spray model would include both the production of spray droplets (i.e., how many are produced at the surface) and the feedback effects of spray on the air in which they are suspended. For spray production, the so-called sea spray generation function (SSGF) governs the droplet size distribution (DSD). It is often assumed that the SSGF is associated with wind speed, although the mechanisms of spray generation vary under different wind speed regimes, for example, bubble-generated versus spume droplets (Ortiz-Suslow et al., 2016; Veron, 2015). In addition to a simple wind speed dependence, recent studies also demonstrate that wind-wave Reynolds number, wave age, wave steepness, significant wave height, and other surface and wave properties could also influence how spray is generated (Anguelova & Bettenhausen, 2019; Brumer et al., 2017; Romero et al., 2017; Salisbury et al., 2013). Thus, different parameterizations yield different expressions for the SSGF. In particular, there is a very wide variability in predicting heavy droplets, namely, droplets with size greater than $\mathcal{O}(200\,\mu m)$ (de Leeuw et al., 2011; Ortiz-Suslow et al., 2016; Veron et al., 2012).

Besides the uncertainties in spray generation, modeling the spray's feedback effects and developing simplified parameterizations of sea spray for momentum, heat, and mass (e.g. moisture and gas) transfer are not simple either. These parameterizations include their own set of assumptions, apart from those governing the SSGF (see, e.g., Andreas et al., 2015; Fairall et al., 1994, 2003; Mueller & Veron, 2014a).

A simple approach to modeling the feedback effects of a spray population whose size range is large and governed by the DSD is to assume that the influence of spray from a specific droplet size is independent from all others. For example, consider the often-used expression (e.g., in Fairall et al., 1994 and Andreas et al., 2015) for sensible heat flux mediated by spray ($Q_{s,sp}$),

$$Q_{s,sp} = \int_{r_1}^{r_2} q(r_0)\frac{dF}{dr_0}dr_0, \tag{1}$$

where $r_1$ and $r_2$ are the limits of the spray size range considered in a model, $q(r_0)$ represents the heat contributed from droplets with the initial size $r_0$, and $\frac{dF}{dr_0}$ is the SSGF. For example, in the bulk spray models of Fairall et al. (1994) and Andreas et al. (2015), $q(r_0)$ is assumed independent from the generation mechanisms as it is multiplied by $\frac{dF}{dr_0}$. A similar treatment is also applied to the Lagrangian models of Edson et al. (1996), Mueller and Veron (2014b), Mueller and Veron (2014a), and Troitskaya et al. (2018), where the total effect is the sum of the contributions from each size over a wide range of spray droplets.

Based on the above assumption, recent high-resolution studies then focus on monodispersed (single-sized) DSDs and investigate the details of spray-mediated air-sea fluxes given a specific spray size (Helgans & Richter, 2016; Peng & Richter, 2017, 2019; Rastigejev & Suslov, 2016, 2019; Richter & Sullivan, 2014). These studies implicitly make the same assumption that each droplet size acts independently from the others when combined. In contrast, only a few studies consider more than one spray size. For example, multiple representative sizes are considered simultaneously in direct numerical simulation (DNS) studies by Tang et al. (2017) and Druzhinin et al. (2018) to investigate the influence of heat flux, and specific (idealized) distributions of particle size are considered in Richter et al. (2016) (uniform distribution) and Pan et al. (2019) (nonuniform distribution). These polydispersed studies begin to demonstrate the inadequacy of the monodispersed assumption, which indicates that particles of one size may indirectly influence how particles of another size interact with the surrounding flow.

Another question associated with the polydispersity of the spray suspension is related to the representative size (if one exists). For example, Andreas et al. (2008,2015) put forward the concept of a single representative size for sensible and latent heat fluxes to simplify the spray flux computation procedures. In these studies, the representative size is selected ad hoc as the size where droplets contribute the most sensible and latent heat flux. In Equation 1, this idea is equivalent to looking for the maximum of $q(r_0)\frac{dF}{dr_0}$, the contribution from a single droplet multiplied with its generation strength. By using a stochastic Lagrangian model, this concept was qualitatively demonstrated by Mueller and Veron (2014a) (cf. Figure 6 in their paper), but the peak of the heat contribution changes according to different SSGFs. Hence, in this study, we also aim to evaluate some straightforward a priori candidates of the representative size of an SSGF for predicting bulk heat and mass transfer in this simplified way.

In the current study, we avoid the uncertainties in the generation mechanisms themselves and focus instead on the physical and thermodynamic interactions between spray and the air, emphasizing the interactions within polydisperse collections of droplets. We continue to take advantage of a high-resolution Eulerian-Lagrangian framework with DNS to resolve the evaporating spray droplets in a simplified surface layer, following previous studies (Helgans & Richter, 2016; Peng & Richter, 2017, 2019). The purpose of the current study is to address and verify untested hypotheses in bulk, upscaled models by using high-resolution simulations that provide fundamental, process-level insight. In this sense, we have matched key nondimensional parameters of the physical system (namely, droplet time scales, concentrations, and settling rates relative to the turbulence), and the dimensional quantities used for the simulations must be interpreted accordingly as not being literal recreations of the high-wind air-sea interface.

The paper discusses the following topics. We first discuss the feasibility of using bulk spray estimates on two-way coupled polydispersed droplet suspensions, where we estimate the individual spray-mediated fluxes associated with each size class and compare with statistics sampled from DNS. Moreover, we also compare the total heat flux ($H_T$) computed from DNS and an improved bulk model (i.e., Equation 3 in
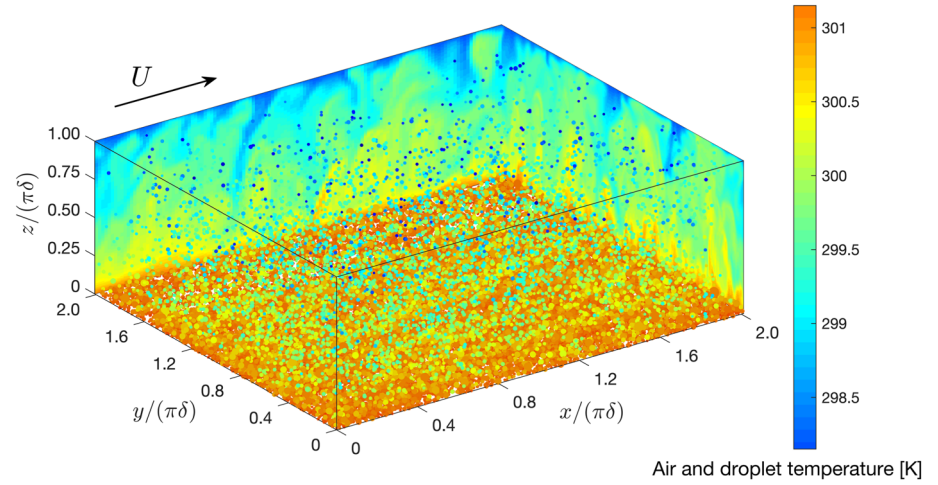
**Figure 1.** Instantaneous temperature and location of droplets. The example has a mass fraction at 5%, and one fifth of the droplets are plotted for clarity. Color represents both air and droplet temperature, and droplets are represented by spherical dots. In the figure, $U$ represents the horizontal mean velocity and $\delta$ is the domain height defined in Table 1.

Peng & Richter, 2019) to assess the necessity of properly accounting for the polydispersity of the DSD. Finally, we test various moments of the DSD to find an approximate representative size of a population of droplets, and we investigate the feasibility and applicability of these approximates by assessing the predicted temperature/moisture fields and spray-mediated heat flux.

## 2. Methodology

In this study, we idealize the complex air-sea interface into a spray-laden turbulent flow over a flat surface to investigate specific features of air-spray interaction. In our DNS model, we simulate an Eulerian carrier phase (air) and a Lagrangian dispersed phase (saline water droplets). For the Eulerian solver, we resolve all scales of turbulent motions; for the Lagrangian droplets, we make the point-particle approximation, which is an appropriate assumption in the droplet size and concentration regimes studied here. A snapshot showing instantaneous flow velocity and droplet positions is provided in Figure 1, and details of the Eulerian and Lagrangian methods are outlined below.

### 2.1. Governing Equations of the Eulerian-Lagrangian Algorithm
### 2.1.1. Carrier Phase

To investigate the lower portion of the atmospheric surface layer, we set up a turbulent open-channel flow driven by a pressure gradient, with temperature and humidity specified at the upper and lower boundaries. Under the Boussinesq approximation, we assume an incompressible turbulent air flow with neutral stability as well as constant viscosity and thermal diffusivity. With these assumptions, the governing equations of mass is given by

$$\nabla \cdot \overrightarrow{\mathbf{u}} = 0, \tag{2}$$

where $\overrightarrow{\mathbf{u}} = (u, v, w)$ is the velocity of the air at location $\overrightarrow{\mathbf{x}} = (x, y, z)$. The momentum equation is given by

$$\frac{\partial \overrightarrow{\mathbf{u}}}{\partial t} + \overrightarrow{\mathbf{u}} \cdot \nabla \overrightarrow{\mathbf{u}} = -\frac{1}{\rho_a}\nabla P + \nu_a \nabla^2 \overrightarrow{\mathbf{u}}, \tag{3}$$

where $\nabla = \left\{ \frac{\partial}{\partial x}, \frac{\partial}{\partial y}, \frac{\partial}{\partial z} \right\}$, $t$ is time, $P$ is the pressure, $\rho_a$ is the air density, and $\nu_a$ is the kinematic viscosity of air (see Table 1 for parameter values).

The air temperature ($T$) and specific humidity ($q = \rho_v/\rho_a$, the ratio of vapor density to the constant dry-air density) of the air are computed via an advection-diffusion equation,

**Table 1**
*Simulation Parameters*

| Parameters | Symbols | Values |
|---|---|---|
| Friction Reynolds number | $Re_\tau$ | 300 |
| Schmidt number | $Sc$ | 0.615 |
| Prandtl number | $Pr$ | 0.71 |
| Density of air | $\rho_a$ | $1.1 \text{ kg m}^{-3}$ |
| Density of water | $\rho_w$ | $1{,}000 \text{ kg m}^{-3}$ |
| Kinematic viscosity of air | $\nu_a$ | $1.537\times10^{-5} \text{ m}^2\text{s}^{-1}$ |
| Specific heat of air | $c_{p,a}$ | $1{,}006 \text{ J K}^{-1}\text{kg}^{-1}$ |
| Specific heat of water vapor | $c_{p,v}$ | $1{,}952 \text{ J K}^{-1}\text{kg}^{-1}$ |
| Latent heat of evaporation | $L_v$ | $2.44\times10^6 \text{ J kg}^{-1}$ |
| Molecular weight of water | $M_w$ | $0.018 \text{ kg mol}^{-1}$ |
| Molecular weight of salt | $M_s$ | $0.0584 \text{ kg mol}^{-1}$ |
| Vertical height of domain | $\delta$ | $0.04 \text{ m}$ |
| Maximum injection displacement | $\delta_{inj}$ | $0.005 \text{ m}$ |

$$\frac{\partial \phi}{\partial t} + \overrightarrow{\mathbf{u}} \cdot \nabla \phi = D_\phi \nabla^2 \phi + \frac{1}{\rho_a} S^\phi, \tag{4}$$

where $\phi = T, q$. For the diffusion term, $D_\phi$ represents the thermal ($\alpha$) or vapor ($D_v$) diffusivity. The thermal diffusivity is defined as $\alpha = \kappa_T/(\rho_a c_{p,a})$, where $\kappa_T$ is the thermal conductivity of air and $c_{p,a}$ is the specific heat of air. These diffusivities are specified by the dimensionless Prandtl ($Pr = \nu_a/\alpha$) and Schmidt ($Sc = \nu_a/D_v$) numbers. The source term $S^\phi$ in Equation 4 represents the two-way coupling between the droplets and air, $S^T$ for temperature (due to heat exchange between the droplet and air), and $S^q$ for the specific humidity (due to evaporation/condensation of the droplet). We omit the momentum coupling between spray droplets and turbulent flow for simplicity so that we can isolate and emphasize the thermal coupling effects and since the mass fractions are sufficiently low that modifications to the turbulence would be low. Detailed expressions of $S^h$ and $S^q$ are documented in Peng and Richter (2017) and Helgans and Richter (2016).

### 2.1.2. Dispersed Phase

Under the point-particle approximation, we introduce the following Lagrangian equations (which do not necessarily align with the grids used for the carrier phase) governing the temporal evolution of position, velocity, temperature, and radius for each particle based on conservation of mass, momentum, and energy. Starting with the instantaneous position ($\overrightarrow{\mathbf{x}}_p$) of a droplet, we update each droplet's velocity

$$\frac{d\overrightarrow{\mathbf{x}}_p}{dt} = \overrightarrow{\mathbf{v}}_p, \tag{5}$$

where $\overrightarrow{\mathbf{v}}_p$ is the velocity for each individual droplet. From momentum conservation, we have the following equation for updating the droplet velocity:

$$\frac{d\overrightarrow{\mathbf{v}}_p}{dt} = (1 + 0.15 Re_p^{0.687})\frac{1}{\tau_p}(\overrightarrow{\mathbf{u}}_f - \overrightarrow{\mathbf{v}}_p) - \overrightarrow{\mathbf{g}}, \tag{6}$$

where $\overrightarrow{\mathbf{v}}_p$ is the velocity of an individual droplet and is dictated by the interpolated fluid velocity ($\overrightarrow{\mathbf{u}}_f$; subscript "$f$" denotes interpolation). Gravity is also considered ($\overrightarrow{\mathbf{g}} = (0, 0, g_z)$) and is nonzero in the vertical direction. The particle Reynolds number (typically very small in the current study) is defined as $Re_p = (2r_p|\overrightarrow{\mathbf{u}}_f - \overrightarrow{\mathbf{v}}_p|)/\nu_a$, and $\tau_p = (\rho_p(2r_p)^2)/(18\nu_a\rho_a)$ is the acceleration time scale of the particle; $g_z$ is the magnitude of gravitational acceleration in the vertical ($z$) direction.

For spray evaporation, the thermodynamic model is based on Andreas (1992), Andreas et al. (1995), Pruppacher and Klett (1996), and Mueller and Veron (2010). Given the density of saline water ($\rho_p$), the mass of droplets $\left(m_p = \frac{4}{3}\rho_p r_p^3\right)$ can be calculated based on the radius ($r_p$) of a spherical droplet, which is governed by the following equation:

$$\frac{dr_p}{dt} = h_m \frac{\rho_a}{\rho_w}(q_f - q_p), \tag{7}$$

where $\rho_w$ is the density of pure water and $q_p$ is the specific humidity at the droplet surface (assuming a saturation pressure which depends on salinity and droplet size; see Helgans & Richter, 2016, for the full expression for $q_p$). The term $h_m$ is the convective mass transfer coefficient of evaporative droplets, so that $h_m = \frac{1}{9}(Sh\rho_p r_p)/(Sc\rho_a\tau_p)$, where $Sh$ is the dimensionless Sherwood number $Sh = 2 + 0.6 Re_p^{1/2} Sc^{1/3}$ (Ranz & Marshall, 1952).

The temperature evolution of droplets is based on the air-droplet sensible and latent heat transfer exchange rates (Andreas, 1990), that is,

**Table 2**
*Boundary Conditions of the DNS*

| BC Groups | $T_{bot}$ (K) | $T_{top}$ (K) | $RH_{bot}$ | $RH_{top}$ | $\Phi_w = m_w/m_a$ | $Re_\tau$ |
|---|---|---|---|---|---|---|
| M1 | 301.15 | 298.15 | 100% | 90% | 1%, 5%, 10% | 300 |
| M2 | 301.15 | 301.15 | 100% | 90% | 5% | 300 |
| M3 | 298.15 | 301.15 | 100% | 100% | 5% | 300 |
| M4 | 301.15 | 298.15 | 98% | 90% | 1%, 5%, 10% | 300 |

*Note.* $T_{bot}$ and $T_{top}$ represent the temperature at bottom and top boundaries, $RH_{bot}$ and $RH_{top}$ represent relative humidity at the two boundaries, $\Phi_w$ is the spray mass fraction, and $Re_\tau$ represents the friction Reynolds number of the flow.

$$\frac{dT_p}{dt} = -\frac{1}{3}\frac{Nu_p c_{p,a}\rho_p}{Pr}\frac{1}{c_L \rho_w \tau_p}(T_p - T_f) + 3L_v\frac{1}{r_p c_L}\frac{dr_p}{dt} \tag{8}$$

where $c_L$ is the specific heat of liquid water (assumed constant) and $L_v$ is the latent heat of evaporation. The first term on the right-hand side of Equation 8 represents sensible heat transfer between the droplet and surrounding air, which is treated as a convective process and driven by the difference between the droplet temperature $T_p$ and the surrounding air temperature $T_f$, whose efficiency is given by the dimensionless Nusselt number (Ranz & Marshall, 1952): $Nu_p = 2 + 0.6Re_p^{1/2}Pr^{1/3}$. Here, $Pr = \nu_a/\alpha = 0.71$ is the Prandtl number of air. The latter term on the right-hand side is associated with evaporation/condensation, which is coupled with Equation 7.

Equation 8 implicitly contains a time scale associated with droplet temperature evolution ($\tau_T$). As discussed in Andreas (1990, 2005) and Veron (2015), at early stages of evaporation, the latent term containing $dr_p/dt$ in Equation 8 is much smaller than the sensible term. Hence, the sensible heat exchange dominates at this stage with an exponential temporal evolution (valid when RH in the air is above 75%; cf. Andreas, 2005). For specifying $\tau_T$, we follow the scaling analysis of Mueller and Veron (2010) given an initial size $r_p = r_0$:

$$\tau_T = \frac{Pr}{Nu_p c_{p,a}\rho_p}\frac{c_L \rho_w}{}\tau_p \propto r_0^2. \tag{9}$$

The time scale associated with radius evolution ($\tau_r$) is usually $\mathcal{O}(10^3)$ times larger than $\tau_T$. We follow the exponential decay time by Andreas et al. (2008, 2015) so that $\tau_r \approx 670\tau_T$ in the current study.

## 2.2. Numerical Configurations and Droplet Generation

In the current study, the turbulent air flow is driven by a pressure gradient in $x$ direction (cf. Equation 3), and its intensity is associated with the corresponding friction Reynolds number $Re_\tau = (u_\tau \delta)/\nu_a$, where $u_\tau$ is the friction velocity and $\delta$ is the domain height (cf. Table 1). We set $Re_\tau = 300$, which is the benchmark $Re_\tau$ in both Peng and Richter (2017) and Peng and Richter (2019), and the influence of $Re_\tau$ has been shown in these previous studies to be minimal for the quantities being measured. Along with periodic boundary conditions in both the streamwise and spanwise directions, no-slip and no-flux conditions are applied on the bottom and top boundaries, respectively. We consider Dirichlet boundary conditions of air temperature and humidity on the top and bottom, which are given in Table 2, where "M1" is the baseline for the study. To test the sensitivity of our conclusions on the boundary conditions, we have considered Cases M2 and M3, which vary the balance between latent and sensible heat transfer across the domain. Note that in this open-channel configuration, the momentum flux varies linearly with height across the domain, while fluxes of sensible and latent heat are constant with height.

For spray droplets, we enforce a constant total number in the domain, as well as a stationary DSD throughout the simulations. When a droplet hits the lower boundary, it is replaced with a droplet with a random vertical velocity and the same initial size of the precedent one at a random location. To mimic the randomness of the spray injection, the injection velocity follows a uniform distribution with a constant maximum velocity that sets a limit of maximum injection displacement (defined as $\delta_{inj}$) which a droplet could travel without turbulence (cf. Table 1).

To initialize droplets for each simulation, the mass of water $m_w$ in the droplet phase is first calculated based on the assigned bulk mass fraction, defined as $\phi_m = m_w/m_a$, where $m_a$ is the mass of air in the domain. In the current study, we select $\phi_m$ ranging from 1% to 10%, where significant changes in the responses of heat fluxes due to spray evaporation can be found and the assumptions of omitting momentum coupling stands valid. At the initialization stage, the total number of size classes ($N_{r_0}$) and their corresponding initial size ($r_{0,i}$ where $i = 1$ to $N_{r_0}$) are defined; so is the SSGF (or DSD) associated with the size classes. Then, a random number is drawn from a uniform distribution ranging from 0 and 1 for each droplet to be generated. The size $r_{0,i}$ that has the closest cumulative probability $\mathcal{F}(r_{0,j})$ to this random number is selected as the droplet radius. The
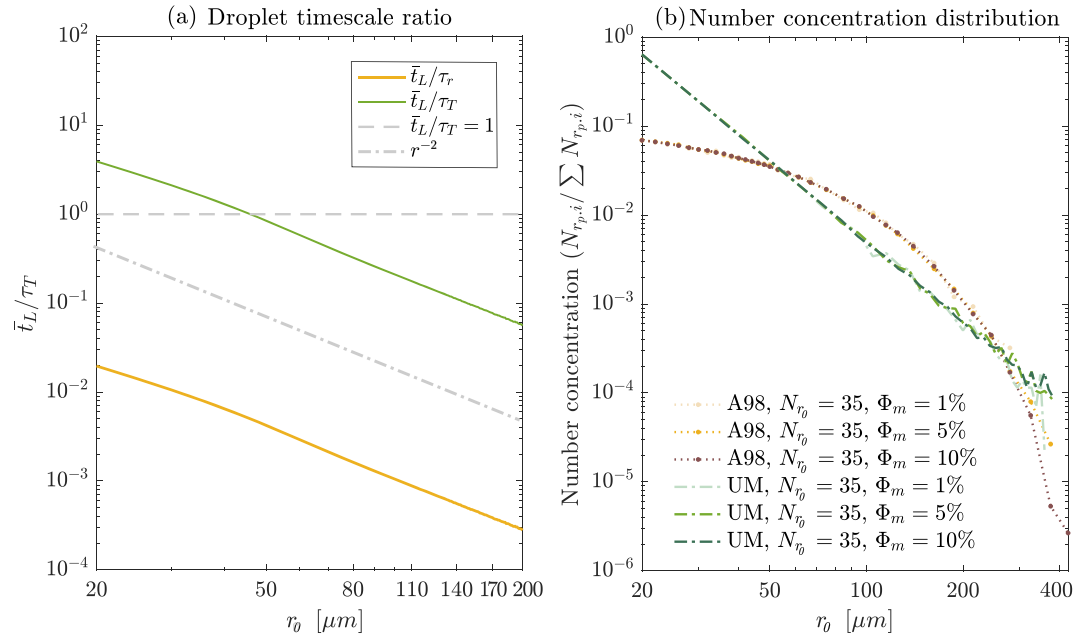
**Figure 2.** (a) Ratios of spray time scales given the initial size ($r_0$) (discussed in section 2.1.2) and (b) number concentration distribution of the initial size ($r_0$) for different SSGFs.

drawing of random number continues as the mass of droplets increases until the total $\phi_m$ reaches the desired value.

## 2.3. Size Distribution

We consider both idealized and realistic DSDs of spray in the current study. In Peng and Richter (2017, 2019), we discuss the different roles of spray by discriminating spray behavior using the ratio of spray time scales, in particular, the ratio of the droplet residence time $t_L$ to its temperature response time $\tau_T$. Note that the radius response time ($\tau_r$), another important spray evaporation time scale, is much larger than $\tau_T$ (Andreas, 1992; Andreas et al., 2015; Veron, 2015); hence, we use $\tau_T$ as a first-choice option for scaling the residence time. For example, large droplets have very short residence times ($t_L$) compared to their thermal response time ($\tau_T$), while small droplets have the opposite. In the current simulation setting, droplets with radius from 20 to 200 μm have corresponding time scale ratios $\tilde{t}_L = t_L/\tau_T$ ranging from $\mathcal{O}(10)$ to $\mathcal{O}(0.1)$. This range of droplet size is ideal for our DNS model to investigate the effects of droplets spanning different behavior regimes. We also neglect the size of large spume droplets (e.g., $r_p > 500$ μm or $\tilde{t}_L \ll \mathcal{O}(0.1)$) to avoid violating the point-particle assumption, though their thermal influence is trivial. In Figure 2a, we plot residence time normalized with different scaling time scales for various initial droplet radii, showing the relationship between residence time and thermal response time scales.

To begin, we consider multiple bidispersed DSDs, each with only two distinct radii selected to represent the various regimes of the dimensionless droplet time $\tilde{t}_L$. Specifically, we identify three droplet radii (25, 50, and 200 μm), representing so-called "small," "medium," and "large" droplets, which lie in three different regimes of $\tilde{t}_L$ as seen in Figure 2. For each bidisperse droplet size combination, three total mass fractions of $\phi_m =$ 1%, 5%, and 10% are considered, and each size contributes half of the total droplet mass. The details are listed in Table 3 under the groups "BD1," "BD2," and "BD3."

To consider more realistic DSDs, the polydispersity of spray droplets are parameterized according to existing SSGF estimates. Specifically, we adopt two commonly used SSGF scalings in the current study: (1) a

**Table 3**
*Configurations of Polydispersed Cases*

| Groups | $N_{r_0}$ | min. $r_0$ (μm) | max. $r_0$ (μm) | SSGF | $\Phi_m$ |
|---|---|---|---|---|---|
| BD1 | 2 | 25 | 50 | — | 1%, 5%, 10% |
| BD2 | 2 | 25 | 200 | — | |
| BD3 | 2 | 50 | 200 | — | |
| U-M (fine) | 331 | 20 | 380 | U-M | |
| U-M (raw) | 35 | 20 | 380 | U-M | |
| U-ML | 24 | 20 | 135 | U-M | |
| U-MR | 27 | 70 | 200 | U-M | |
| A98 | 35 | 20 | 425 | A98 | |

power law scaling of droplet number with radius $r_0^{-3}$, reflecting a uniform distribution of droplet mass which is observed in the laboratory experiments of Ortiz-Suslow et al. (2016) for droplets ranging from 80 to 1,400 $\mu$m (hereafter "UM") and (2) an exponential decay of droplet number with radius derived by Andreas (1998) which is further simplified by Troitskaya et al. (2016) (hereafter "A98"). Mathematically, the corresponding SSGFs ($S_n$) are expressedas

$$S_n(r_0) = \begin{cases} C_1 r_0^{-3} & \text{UM,} \\ C_2 \left(\dfrac{U_{10}}{u_0}\right)^d \exp(-\chi r_0) & \text{A98,} \end{cases} \tag{10}$$

where $U_{10}$ is the 10-m wind velocity (selected to be 40 m/s in the current study), and the remaining fitting coefficients are set as $d = 0.01*(U_{10}-40)+5.5 = 5.5$ and $\chi = 0.023$ (Troitskaya et al., 2016). In this study, we adopt the scaling of the SSGF but control the total mass of droplets in a simulation. Hence, $C_1$ and $C_2$ in Equation 10 are chosen to assign the desired overall mass fraction. Note that, as mentioned above, we do not claim that the dimensionalwind speeds found in the DNS are consistent with 40-m/s winds; instead, we aim to investigate droplet concentrations and distributions which are relevant at high winds but in a scaled DNS setting where Reynolds number is limited by computational resources. In Figure 2b, we show the normalized number distribution of the two SSGFs given various droplet mass loading, which is sampled stochastically from Equation 10 during the initialization stage.

Given the strength of droplet generation in Equation 10, one can express the probability of droplet generated $\mathscr{P}(r_{0,i})$ for each size class $i$ discretely a

$$\mathscr{P}(r_{0,i}) = \frac{S_n(r_{0,i})}{\sum_{i=1}^{N_{r_0}} S_n(r_{0,i})}, \tag{11}$$

with the cumulative probability ($\mathscr{F}(r_{0,j})$) for each size class given as $\mathscr{F}(r_{0,j}) = \sum_{j=1}^{i} \mathscr{P}(r_{0,j})$, where $j$ ranges from 1 to $i$ and $i$ from 1 to $N_{r_0}$.

## 2.4. Partitioning Air-Sea Heat Fluxes and the Bulk Algorithms

To study the effects of spray on heat fluxes and using the same conceptual framework of Fairall et al. (1994), we partition the total air-sea heat flux ($H_T$) into interfacial (subscript "$int$") and spray-mediated components (subscript "$sp$") for sensible (subscript "$s$") and latent (subscript "$L$") fluxes. Moreover, we can further partition each interfacial flux into two additional components: the turbulent flux (subscript "$turb$") and diffusive flux (subscript "$diff$") by Reynolds averaging Equations 3 and 4. The total heat flux can therefore be expressed according to the following expressions:

$$\begin{aligned} H_{s,total}(z) &= H_{s,turb}(z)+H_{s,diff}(z)+H_{s,sp}(z) \\ &= \rho_a c_{p,a}\langle w'T'\rangle - \rho_a c_{p,a}\alpha\frac{d\langle T\rangle}{dz} + \sum_{i=1}^{N_{r_0}}\left[-\int_0^z c_{p,a}S_{r_{0,i}}^T(z)dz\right], \end{aligned} \tag{12}$$

and

$$\begin{aligned} H_{L,total}(z) &= H_{L,turb}(z)+H_{L,diff}(z)+H_{L,sp}(z) \\ &= (c_{p,v} + h_v^0)\left\{\rho_a\langle w'q'\rangle - \rho_a D_v\frac{d\langle q\rangle}{dz} + \sum_{i=1}^{N_{r_0}}\left[-\int_0^z \rho_a S_{r_{0,i}}^q(z)dz\right]\right\}. \end{aligned} \tag{13}$$

In Peng and Richter (2019) and Helgans and Richter (2016), we define each term in Equations 12 and 13based on their role in the governing equations of the system. Note that in this study, we extend the spray-mediated heat fluxes by computing the individual components of the heat/moisture source terms ($S_{r_{0,i}}^T$ and $S_{r_{0,i}}^q$, respectively) for each spray size class denoted by their initial radii ($r_{0,i}$). This is then summed over the number of particles for each corresponding size class ($N_{r_0}$) in Equations 12 and 13 (last term on the right-hand side). Angle brackets denote horizontal and time averaging, and primes denote fluctuations off of the mean. The quantity $h_v^0 = 2383 \times 10^3$ J kg$^{-1}$ is a reference enthalpy (Helgans & Richter, 2016).

Correspondingly, as a counterpart to the DNS-calculated spray-mediated heat fluxes, one can write a bulk estimate of the spray flux using the expressions in Fairall et al. (1994):

$$\hat{H}_{s,sp}(r_{0,i})=Q_s(r_{0,i})-Q_L(r_{0,i}), \tag{14}$$

and

$$\hat{H}_{L,sp}(r_{0,i})=Q_L(r_{0,i}), \tag{15}$$

where the hat denotes the bulk-estimated values of heat fluxes, which is calculated from $\bar{Q}_s$ and $\bar{Q}_L$—the estimates of the spray exchange rate for sensible and latent heat (i.e., the nominal fluxes given an expected temperature and radius change for the droplets; see Fairall et al., 1994). Thus, for each size, we expand the statistics associated with spray in Equations 8 and 9 of Peng and Richter (2019) as

$$Q_s=\sum_{i=1}^{N_{r_0}}Q_s(r_{0,i})=-\sum_{i=1}^{N_{r_0}}c_p m_{p,i}\Delta T_{p,i}(F_i/A), \tag{16}$$

and

$$Q_L=\sum_{i=1}^{N_{r_0}}Q_L(r_{0,i})=-\sum_{i=1}^{N_{r_0}}L_v \Delta m_{p,i}(F_i/A), \tag{17}$$

where $\Delta T_{p,i}$ and $\Delta m_{p,i}$ are the expected values of temperature and mass change for droplets in size class $i$, $F_i$ is the replenishment rate of droplets at the bottom surface, and $A$ is the horizontal sampling area of the simulation domain. Hence, by applying Equation 19 of Peng and Richter (2019), we have a bulk estimate for the total heat fluxes given by

$$H_T=H_{T,0} + \sum_{i=1}^{N_{r_0}}\left[Q_{s,i} + \gamma Q_{L,i}\right], \tag{18}$$

where, according to Peng and Richter (2019), $\gamma=-0.74$. This is the baseline model assuming independent contributions from the different spray size classes; we will critically assess this assumption in the following sections.

## 3. Results

In this section, we discuss how distinct droplet sizes can indirectly influence each other via interactions with the background temperature and humidity fields (via two-way couplings). Then, we apply existing bulk estimates of spray-mediated heat transfer to the bidispersed and polydispersed simulations and assess the assumption of each spray size's independent contribution to the total flux, as presented in Equation 18.

### 3.1. Statistics of the Droplet Temperature and Radius Change

As seen in Equations 14,15, and 18, bulk models rely on the statistics of droplet lifetime and net temperature/radius change to evaluate the spray-mediated heat fluxes. Thus, the average values of $\Delta T_p$ and $\Delta r_p$ are essential for capturing the sensible and latent heat predicted by bulk models. In this section, we discuss the influence of the size distribution on the statistics of $\Delta T_p$ and $\Delta r_p$.

#### 3.1.1. Bidispersed Cases

In Figure 3, we compare the mean temperature ($\Delta T_p$, first row) and mean radius changes ($\Delta r_p$, second row) for bidispersed and monodispersed DSDs. In each panel, the solid lines are the monodispersed cases with the half mass of the bidispersed cases, and the markers represent the bidispersed cases. Cases with different mass fraction $\phi_m$ are denoted by colors. For example, in panel (a), the mass fraction of the monodispersed case at $25\,\mu m$ is $\phi_m=0.5\%$, which is the mass fraction of only the 25-$\mu m$ droplets in the bidispersed cases.

In Figure 3, one can notice that the effects of mixing with a different size becomes noticeable on droplet statistics as mass fraction increases, in particular for medium-size droplets (with $r_0=50\,\mu m$). For example, both $\Delta T_p$ and $\Delta r_p$ for 50-$\mu m$ droplets in bidispersed DSDs (markers) depart from the solid lines
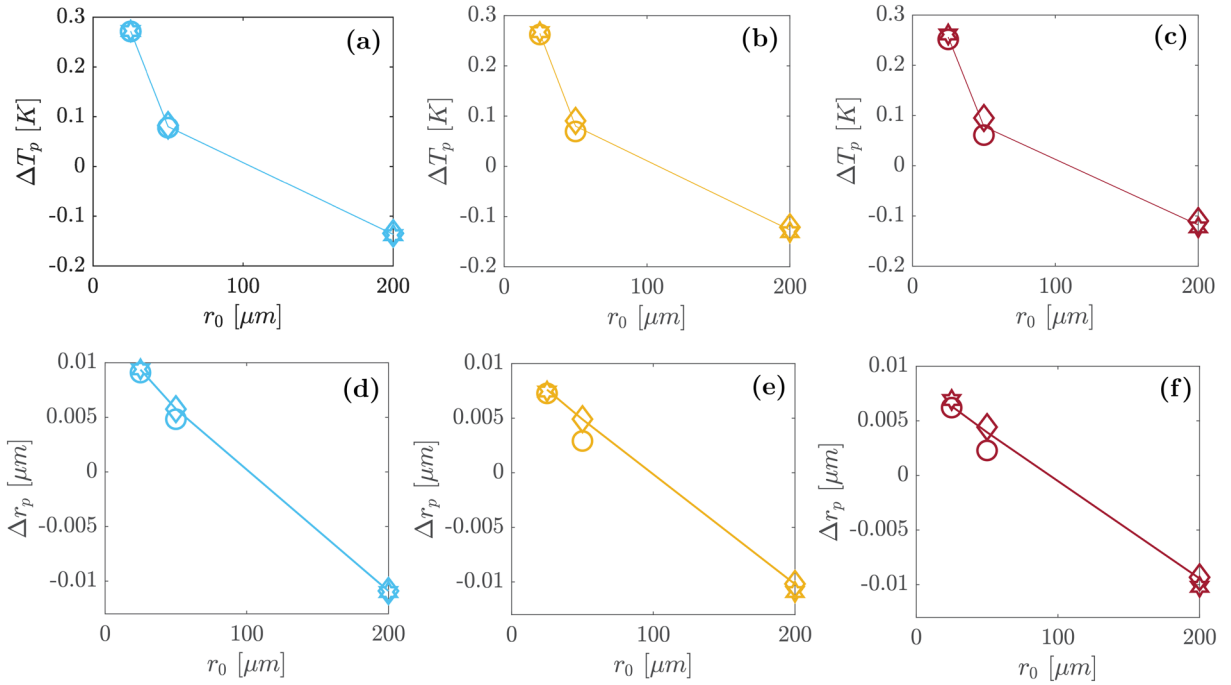
**Figure 3.** $\Delta T_p$ and $\Delta r_p$ for bidispersed cases (markers) and monodispersed cases (lines). Three mass fractions are plotted with various colors: panels (a) and (d): $\Phi_m$=1%; panels (b) and (e): $\Phi_m$=5%; panels (c) and (f): $\Phi_m$=10%. Note: in each panel, two identical markers represent the two radii in a bidispersed case, that is, (i) circles: 25 μm + 50 μm, (ii) hexagrams: 25 μm + 200 μm, and (iii) diamonds: 50 μm + 200 μm.

representing the monodispersed cases. According to Figure 2a, 50-μm droplets have $\tilde{t}_L \approx O(1)$, and we focus on this size in particular in later discussions. In comparison, for small droplets (e.g., 25 μm) or large droplets (e.g., 200 μm), $\Delta T_p$ and $\Delta r_p$ remain arguably unchanged between the bidispersed and monodispersed cases.

In addition, we observe that the variation of $\Delta T_p$ and $\Delta r_p$ depends on the size of droplets which they are mixed with. For example, when mixing with 25-μm droplets, $\Delta T_p$ of 50-μm droplets decreases compared to the monodispersed value (solid lines). This is enhanced with increasing mass fraction. The opposite occurs when the medium droplets coexist with large droplets, for example, cases with 50- and 200-μm droplets (diamonds in panels (c) and (d) in Figure 3): $\Delta T_p$ and $\Delta r_p$ of 50-μm droplets slightly increase compared to monodispersed value, although the trend is not as significant as the scenario of 50-μm droplets mixed with 25-μm ones. Following the definition of $\tilde{t}_L$, it is argued that evaporation for droplets with time scales associated with 50-μm droplets are more susceptible to the ambient conditions compared to other sizes. Droplets with $\tilde{t}_L \approx 1$ (50 μm) can exchange a certain amount of heat and moisture with the ambient air, while $\tau_T$ is not short enough for 50-μm droplets to respond to the local temperature and humidity changes associated with the lower boundary. However, small droplets ($\tilde{t}_L = t_L/\tau_T \gg \mathcal{O}(1)$), such as those with radii of 25 μm, can significantly change the air temperature by redistributing sensible and latent heat; however, their temperature when entering the water depends on the local boundary conditions rather than its initial conditions (Peng & Richter, 2019). Large droplets ($\tilde{t}_L \ll \mathcal{O}(1)$; 200 μm), meanwhile, have large thermal inertia, so their role is to simply warm the ambient during their short residence time (Mueller & Veron, 2014b; Peng & Richter, 2017) by an amount much smaller than 50-μm droplets.

Overall, comparing statistics between bidispersed and monodispersed scenarios reveals the potential consequences of interactions between different sizes in particular at appreciable spray concentration. We will discuss a more general size distribution in the following section for polydispersed DSDs.
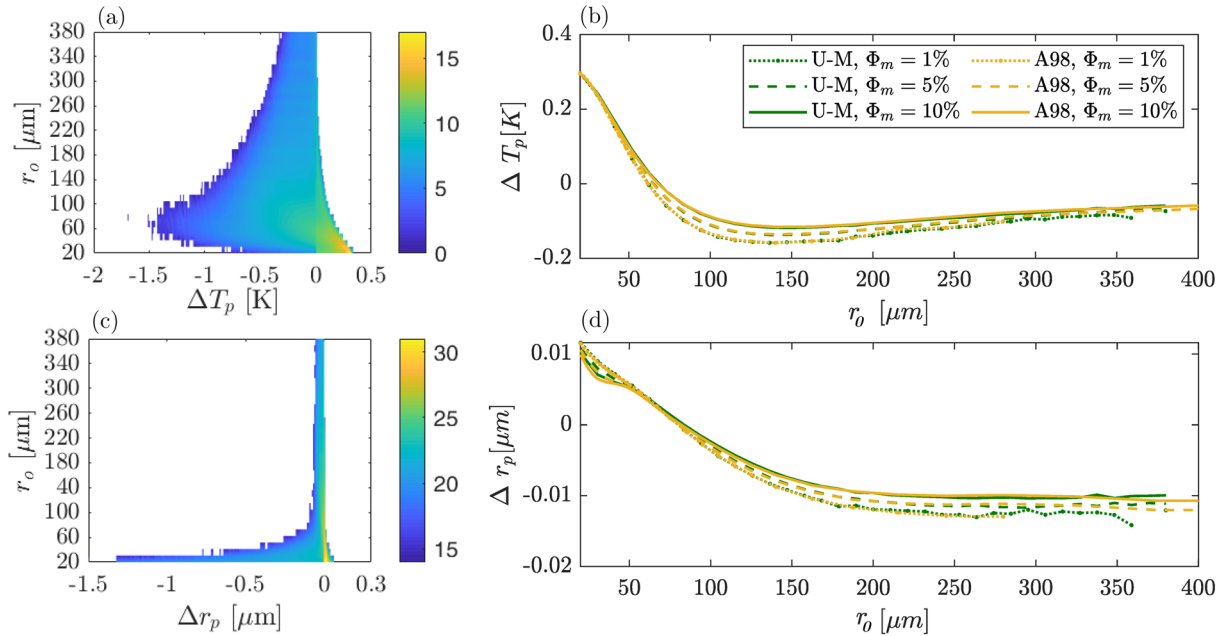
**Figure 4.** Statistics of droplet temperature change ($\Delta T_p$) and radius change ($\Delta r_p$) as a function of initial droplet radius under different droplet mass loading and DSDs. In the left column, subplots (a) and (c) show the 2D-PDF for the U-M (raw) case and $\Phi_m=5\%$, color represents the joint probabilistic density in natural log scale; in the right column, subplots (b) and (d) show the mean $\Delta T_p$ and $\Delta r_p$ for both U-M and A98 cases with different $\Phi_m$.

### 3.1.2. Polydispersed Cases

Similar to the above discussion for bidispersed DSDs, we evaluate the droplet $\Delta T_p$ and $\Delta r_p$ for the uniform-mass DSDs as a complement to Figure 3. Again, we measure the change in droplet temperature ($\Delta T_p$) and radius ($\Delta r_p$) throughout its residence time for all sizes. In Figure 4, we plot the 2-D probability density functions (PDFs) sampled in the simulations for varying $r_0$ (subplots (a) and (c), in log color-scale), and in panels (b) and (d), the mean values of $\Delta T_p$ and $\Delta r_p$ are plotted against the droplets' initial size $r_{0,i}$.

From the 2-D PDFs, one can see that smaller droplets (e.g., $r_0<50\,\mu m$) have more skewed distributions in $\Delta T_p$ and $\Delta r_p$, as one can observe from the high-density region in the lower part of panels (a) and (c). This high-density region, in fact, is indicative of the local effects of the boundary conditions on droplet statistics—an effect which has been discussed in Peng and Richter (2019).

As for the mean temperature change $\Delta T_p$, panels (b) and (d) in Figure 4 show a similar story as that in Figure 3. We observe that the transition zone between positive and negative $\Delta T_p$ is around $r_0\approx70\,\mu m$, which has a corresponding $\tilde{t}_L=t_L/\tau_T$ of $\mathcal{O}(1)$ in Figure 2a. This occurs for similar reasons as that discussed in the previous section and in Peng and Richter (2019), where droplets with radii greater than about $70\,\mu m$ are cooled (relative to their initial temperature) when returning to the surface, while smaller droplets (with $r_0<\mathcal{O}(70\,\mu m)$) have a positive $\Delta T_p$ due to the local effect from the boundary conditions.

In terms of the polydispersity, there exist different sensitivities in the mean $\Delta T_p$ with different total mass fractions ($\phi_m$) and DSDs, where DSDs tend to have weaker influences on spray statistics for all sizes compared to $\phi_m$, given lines with different color overlap at the same mass fraction. We observe that droplets with size ranging from 25 to $50\,\mu m$ have overlapping $\Delta T_p$ and $\Delta r_p$, regardless of the mass fraction or DSD. As the droplet size increases, the sensitivity to mass fraction of $\Delta T_p$ becomes more significant, and eventually, droplets become too big to change their temperature (hence the plateau). Hence, one can observe local minima of the magnitude of $\Delta T_p$ occurring around $\mathcal{O}(100\,\mu m)$ (i.e., $\tilde{t}_L$ ranges between $\mathcal{O}(1)$ and $\mathcal{O}(0.1)$), indicating an optimal size range for droplet releasing sensible heat. Regarding the mean radius change $\Delta r_p$, when the
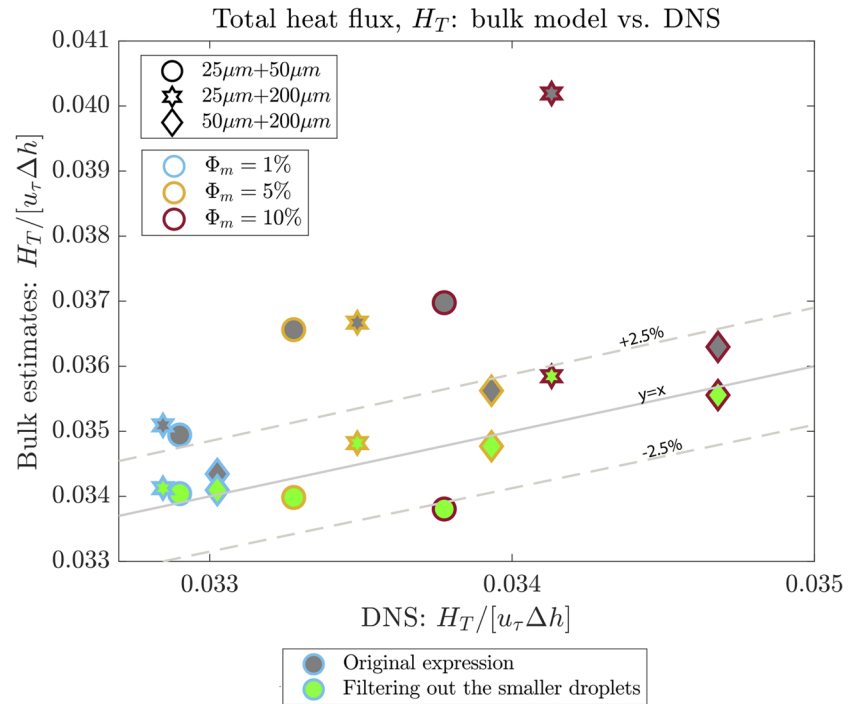
**Figure 5.** Bulk estimate of $H_T$ versus the DNS computed values for bidispersed DSDs. Shapes of markers indicate different size combinations, and edge colors of markers indicate the total mass fraction ($\Phi_m$) affiliated with each simulation. Markers filled in gray use the original expression shown in Equation 18, and markers filled in green filter out the smaller size between the two sizes in a simulation. Note: Results shown by green filled markers are sampled from bidispersed cases, but only contributions of the larger size are considered. Solid gray line indicates the 1:1 line for agreement between DNS and the bulk estimate, and dashed gray lines are ±2.5%.

droplet size increases, one can see a similar trend, except that $\Delta r_p$ levels off at about 250 μm in the current simulation configurations.

To summarize, we observe that the two essential droplet statistics for quantifying sensible and latent heat flux in bulk models, $\Delta T_p$ and $\Delta r_p$, are influenced by polydispersed size distributions. Combining the results from bidispersed and polydispersed simulations, we find that a specific size class can be regarded as the "recipient" of influences from other size classes. For temperature change, droplets from the two ends of the size spectrum tend to be consistent in $\Delta T_p$ with various mass fractions (though the reasons are different), leaving the droplets ranging from 50 to 200 μm as the "recipients" from other radii. Similarly, for radius change, droplets greater than 100 μm tend to be the "recipients" of the influences from the smaller size that has a weaker sensitivity on $\Delta r_p$. Thus, the statistics of how much droplets change temperature and radius suggest the existence of indirect interactions between droplet size classes. Hence, independent contributions from sea spray may not be a justified assumption in bulk models where all transport processes are lumped into the net changes of droplet radius and temperature.

### 3.2. Bulk Estimates of Heat Fluxes
### 3.2.1. Overestimation of the Total Heat Flux in Bulk Algorithms

In this section, we discuss the assumption that the interaction of droplets is negligible for bulk models (e.g., Fairall et al., 1994; Andreas et al., 2015). Equation 18 is an updated formulation of the model of Fairall et al. (1994) tuned by our monodispersed DNS results; a bulk estimate of total heat flux relies on accurate estimates of $\Delta T_p$ and $\Delta r_p$ to predict spray-mediated heat fluxes. To test the negligibility of spray interactions, we compare the total heat flux $H_T$ directly calculated by DNS ($x$ axis) with the results using Equation 18 with the droplet statistics directly sampled from the DNS ($y$ axis). Figure 5 presents this for the bidisperse cases, and Figure 6 presents the comparison for the polydisperse cases. In both figures, the initial comparison is
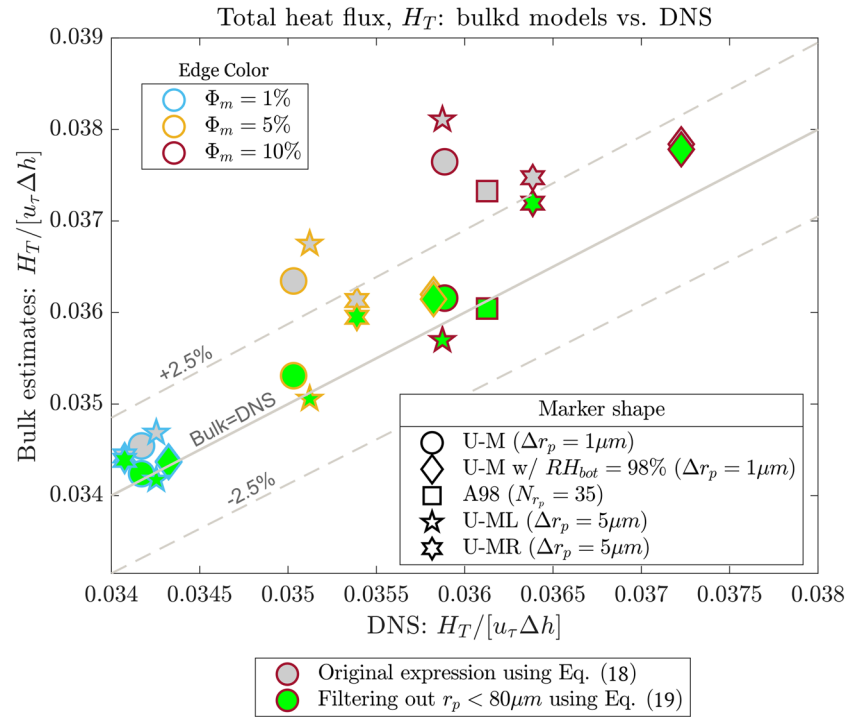
**Figure 6.** Bulk estimate of $H_T$ versus the DNS computed values for polydispersed DSDs. Markers filled in gray use the original expression shown in Equation 18, and markers filled in green filter out droplets smaller than $80\,\mu m$ in a simulation using Equation 19.

indicated with markers filled in gray. When assuming no interaction between droplets of different sizes, Equation 18 should accurately predict the total fluxes according to Peng and Richter (2019). However, we observe significant errors in predicting the total heat flux in both figures.

First, for the bidispersed cases, we observe in Figure 5 that most predictions (in gray) overestimate $H_T$, while this kind of overestimation does not exist in the monodispersed cases, as shown in Peng and Richter (2019). In particular, for the case consisting of 25+200-μm droplets at high $\phi_m$ (i.e., dark red hexagrams filled in gray), one can observe an error of up to 15.5%. Hence, interactions between droplet sizes may need to be considered when mixing with multiple sizes. However, the original model (Equation 18) works properly on the cases which contain no small (25-μm) droplets (e.g., diamonds filled in gray).

We then apply Equation 18 to the polydispersed cases and observe similar behavior for the bulk estimate of $H_T$ in Figure 6. Among the four DSDs provided in Table 3, we observe that, given the same boundary conditions, cases with the U-MR DSD (a truncated version of the U-M DSD) have the least error at each mass fraction, where all droplets have an initial radius greater than $70\,\mu m$. We thus conclude that by observing the errors in Figures 5 and 6, the overestimates of $H_T$ are a result of the interaction of droplets between different size classes. Specifically, small droplets, as defined by their time scale ratio $\tilde{t}_L$, lead to an overestimate in the total predicted heat flux of the mixture.

As discussed in Peng and Richter (2017), small droplets (i.e., those with very short $\tau_T$) can significantly modify the air temperature and humidity in the local regions they reside within. Larger droplets, however, are limited in their modifications to air temperature and humidity due to their slower response time and relatively short lifetime. At the same time, as discussed by Peng and Richter (2019) and Mueller and Veron (2014b), $\Delta T_p$ and $\Delta r_p$ for small droplets are determined by the temperature and humidity field near the bottom boundary immediately before reentry; this is also the region where larger droplets dominate the overall mass concentration. Hence, larger droplets could indirectly influence the prediction of $\Delta T_p$ and $\Delta r_p$ for small droplets, potentially leading to double-counting the feedback from small droplets and thus overestimating $H_T$.

For completeness, we also test another group of simulations with a lower boundary condition of $RH$=98% using the "U-M" DSD (listed as "M4" in Table 2), since this is closer to the saturation RH with typical ocean salinity (Andreas, 1989; Zeng et al., 1998). We find smaller errors introduced for this value of $RH_{bot}$ by using Equation 18, since latent heat released from smaller droplets causes the oversaturation seen in Figure 4. However, since we are investigating whether the original model can capture the influences of short-time processes near the bottom surface for a given size spectrum, we continue discussing simulations with $RH_{bot}$=100% to compare the two models given by Equations 18 and 19.

Considering that small droplets tend to have a net thermodynamic cancelation which redistributes the total heat fluxes (Peng & Richter, 2017), in Figure 5, we try to reevaluate the bulk estimate by removing the contribution from smaller droplets. This is done by setting the corresponding mean rate droplet replacement in the simulations as $F_i$=0 (cf. Equations 14 and 15). Hence, we put forward the following tentative correction to Equation 18 for the bulk model, in order to eliminate the double-counting issue described above:

$$H_T = H_{T,0} + \sum_{i=1}^{N_{r_0}} \mathscr{H}(-\log \tilde{t}_L)\left[\beta Q_{s,i} + \gamma Q_{L,i}\right], \tag{19}$$

where $\mathscr{H}(x)$ is the Heaviside step function, which is equal to 1 when $x \geq 0$. As defined previously, $\tilde{t}_L = t_L/\tau_T$ is the time scale ratio, while $\beta$ is set to 1, and $\gamma$=−0.74 (Peng & Richter, 2019). The updated results applying Equation 19 are plotted in both Figures 5 and 6, indicated by markers filled with green.

For the bidispersed cases, removing the contribution from small droplets significantly improves the prediction quality for cases with 25+200 μm-droplets (hexagrams). In particular, this method works well at high $\phi_m$, where errors for all three cases are reduced to ±2.5%. The correction by filtering out the smaller droplets also works for cases with 50 and 200 μm, where the errors after the correction approached within ±0.5%. However, for cases with 25+50 μm-droplets, although removing the 25-μm droplets improves the issue of overestimates, it also causes an underestimate of $H_T$ at high $\phi_m$ (dark red circles), indicating that the interaction between small and medium droplets is more complex than the combination of small and large droplets.

For the polydispersed cases, in Figure 6, we again observe that filtering out the contribution of small droplets significantly reduces the error. In particular, at a high mass fraction, the errors are also significantly reduced for $RH_{bot}$=100%. For cases with $RH_{bot}$=98%, we find that errors are minimized when filtering out droplets with radii below a threshold of roughly 80 to 100 μm with an optimal result at $r_p$=100 μm (not plotted here). This suggests a net-zero influence from smaller droplets. Comparing the two boundary conditions, since the efficiency of spray evaporation/condensation in the vicinity of the water is changed by varying $RH$, the balance between $t_L$, $\tau_T$, and $\tau_r$ can be changed based on Equation 4. In both cases, Figure 6 suggests an artificial "double-counting" for small droplets.

### 3.2.2. Assessing Bulk Estimates on Spray-Mediated Fluxes

Recall that in Equations 14 and 15, the sensible and latent spray-mediated heat fluxes are calculated based on $\Delta T_p$ and $\Delta r_p$. In this section, we examine the bulk estimates of the spray-mediated heat fluxes (as opposed to the total heat fluxes). In Figure 7, we plot the ratio between bulk estimates and DNS results of total spray-mediated heat flux ($H_{sp}$) and its sensible and latent components at the surface ($z$=0) against the droplet initial radius for the U-M DSD. As one can see, the ratios between the bulk estimates and DNS for the spray-mediated heat fluxes are not always equal to 1, indicating again that the bulk estimate does not work for all sizes.

For example, for the total spray-mediated heat flux $H_{sp}$ (Figure 7, top panel), the bulk estimates are fairly accurate for droplets below 50 μm (where results are plotted near the dashed reference lines). Above, we have discussed that the ratio of droplet residence time and temperature response time, $\tilde{t}_L = t_L/\tau_T$, indicates whether or not droplets are expected to enter a quasi-steady equilibrium stage of evaporation. Considering the original reasoning of the models of Fairall et al. (1994) and Andreas (1990), using $\bar{Q}_s$ to approximate $H_{sp}$ is based on the assumption of an instantaneous adjustment to the ambient air. Hence, it is not surprising that the bulk model provides a good result for $r_0$<50 μm (with $\tilde{t}_L > O(1)$). However, the bulk model slightly
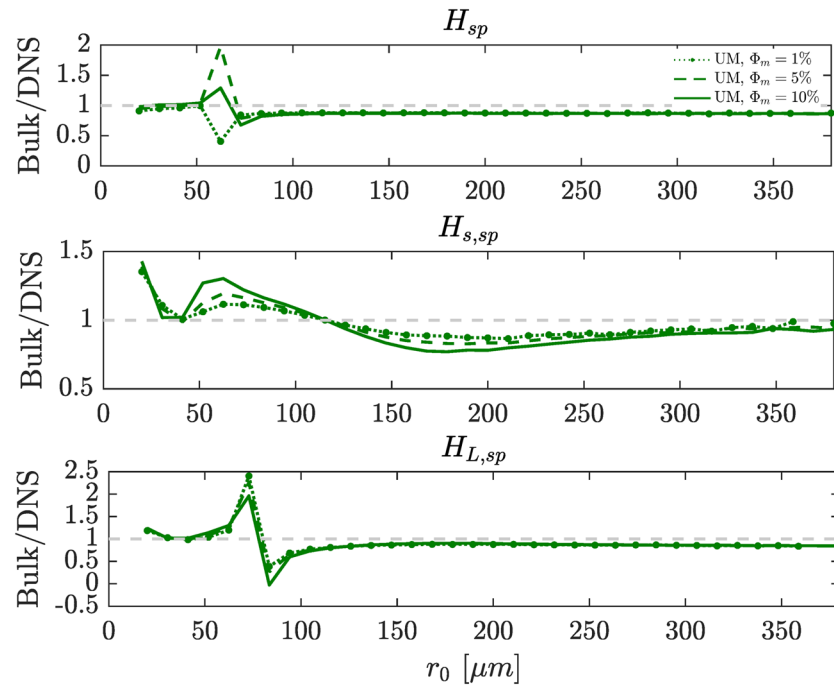
**Figure 7.** Spray-mediated heat fluxes: the ratio between the bulk estimates and DNS results as a function of initial droplet for the three mass fractions of the U-M DSD ($N_{r_0}=35$). If the ratio between bulk-estimated value and DNS results is great than 1, it indicates an overestimate by the bulk models.

underestimates the $H_{sp}$ for droplets larger than 70 μm, and the ratio between bulk estimates and DNS results is about 0.9, although it is still in the range of $\mathscr{O}(1)$.

Between 50 and 70 μm, bulk estimates of the total spray-mediated heat flux $H_{sp}$ in this size range incur significant errors, where the magnitude of the ratio of bulk and DNS values depart from one another. We explain the incorrect bulk estimates in this regime as a matter of time scale as well. In Figure 2, one can see that $\tilde{t}_L$ for this range is $\mathscr{O}(1)$. Hence, droplets in this range have very small $\Delta T_p$ and $\Delta r_p$ as seen in Figure 3. As expected, the spray-mediated heat fluxes $H_{s,sp}$ and $H_{L,sp}$ at the bottom surface are also small compared with small droplets. As a result, when dividing the two values, due to the small value from DNS in the denominator, the ratios are amplified.

In contrast to the total spray-mediated heat flux $H_{sp}$, the bulk model is even more problematic for predicting the sensible spray-mediated flux $H_{s,sp}$. First, for the small droplets, it overestimates $H_{s,sp}$, where one observes a significant error (exceeding 40%) for 20-μm droplets. For droplets larger than about 125 μm, an underestimate occurs, while the extent of the underestimate reaches a local maximum between 150 and 200 μm, and then gradually recovers back to an accurate estimate. For the latent spray-mediated heat flux ($H_{L,sp}$), we see a similar trend to the total spray-mediated flux $H_{sp}$, which has less sensitivity to the mass fraction than the sensible counterpart $H_{s,sp}$. We also observe that the errors between 50 and 100 μm are still significant.

To summarize, due to the assumptions regarding the individual spray-mediated sensible and latent heat flux components, the bulk models will likely not work for all sizes of spray droplets across the relevant spectrum. In particular, these models become problematic in estimating the latent spray-mediated heat flux ($H_{L,sp}$) when droplets have a residence time that is equivalent to the temperature adjustment time. Hence, the models result in a poor performance in this size range for the total spray-mediated heat flux ($H_{sp}$) as well. These discrepancies should be considered for quantifying uncertainties in modeling studies on spray effects following Fairall et al. (1994) (e.g., Garg et al., 2018; Van Eijk et al., 2001).

**Table 4**
*Polydispersed Cases (With Uniform-Mass DSDs) and Their Representative Sizes Based on Equation 20 for Different Size Ranges*

| SSGF | Size range | $\langle r_p \rangle_{(1)}$ | $\langle r_p \rangle_{(2)}$ | $\langle r_p \rangle_{(3)}$ |
|---|---|---|---|---|
| UM-narrow | 20–200 | 36.0 | 42.7 | 52.2 |
| UM-medium | 20–250 | 36.6 | 44.7 | 56.6 |
| UM-wide | 20–380 | 37.0 | 48.1 | 65.6 |

*Note.* Unit: μm.

### 3.3. Representative Droplet Sizes of a Continuum Size Distribution

The bulk models referred to above (e.g., Andreas et al., 2015; Fairall et al., 1994) require integrating individual spray size contributions over a wide range of radius. Hence, a further simplification that has been used in the past (Andreas et al., 2008, 2015; Garg et al., 2018; Mueller & Veron, 2014a; Rastigejev & Suslov, 2016) is to attempt to use a single droplet size which somehow represents the effect of the entire DSD. This is done either based on the shape of the DSD itself or through heuristic arguments about which droplet likely contributes the most to the spray-mediated fluxes (Andreas et al., 2008).

In reality, however, droplet inertia and gravitational settling result in sharp differences in concentration along the vertical direction, which indicates that the SSGF parameterized at the ocean surface may not reflect the size distribution for the majority of the lower MABL (i.e., the surface layer). For example, the largest droplets can only be transported upward away from the lower domain by strong turbulent bursts, which in turn depends largely on the flow within the wave boundary layer (Druzhinin et al., 2017, 2018; Richter et al., 2019; Troitskaya et al., 2018).

Considering a wide size spectrum of spray droplets, unless all droplets are dispersed by turbulence in the same way and play the same role in heat fluxes across the MABL, using a single representative size may introduce additional errors. Thus, we use our DNS framework to explore whether or not there exists a single representative droplet size for a given DSD. In this section, we test three representative sizes based on the U-M DSD using the M1 setup in Table 2.

#### 3.3.1. Polydispersity and the Representative Size of SSGFs

Three representative sizes are considered in this section, and they are based on the arithmetic mean, square-root mean, and cubic-root mean of the distribution, respectively (i.e., first, second, and third moments of the DSD). The three different mean values indicate whether or not the droplet contribution to the heat flux depends on abundance (i.e., concentration), surface area, or volume/mass, respectively. Specifically, given $n=1,2,3$, one can write the representative sizes as

$$\langle r_p \rangle_{(n)} = \left( \frac{\sum_{i=1}^{N_p} r_p^n}{N_p} \right)^{\frac{1}{n}}, \tag{20}$$

where $N_p$ is the total number of droplets given a specific size distribution and mass fraction. Applying Equation 20 to the U-M SSGF, we calculate the representative sizes given the narrow, medium, and wide size ranges listed in Table 4.

#### 3.3.2. Comparisons of Air Temperature, Humidity, and Heat Fluxes

In Figure 8a, we plot the vertical profiles of local volume-weighted average of droplet size using solid lines for the three size ranges listed in Table 4. The dashed vertical lines in Figure 8a indicate the three representative moments of the overall size distribution, that is, $\langle r_p \rangle_{(i)}$ (with $i=1,2,3$) shown in Equation 20. Clearly, large droplets tend to remain near the bottom boundary, as expected. Within the maximum injection height $\left( \delta_{inj} = \frac{1}{8}\delta \right)$, the volume-weighted mean radius is much larger than $\langle r_p \rangle_{(3)}$ due to the presence of a large number of heavy droplets. However, the volume-weighted mean radius above the spray layer is smaller than 35 μm, which is slightly smaller to the value of the arithmetic mean $\langle r_p \rangle_{(1)}$. Besides, despite the different size ranges, the mean size for these three DSDs above $\delta_{inj}$ quickly converges, which are invariant to the difference in the concentration of heavy droplets.

To compare the response of the air temperature and humidity fields to the three candidate representative droplet sizes, Figures 8b and 8c show the vertical profiles of air temperature ($T$) and relative humidity ($RH$) using monodisperse DSDs with radii equal to the three radii in Table 4. These are compared to the temperature and $RH$ of the UM-medium polydisperse DSD. We find that the volume-weighted $\langle r_p \rangle_{(3)}$ successfully predicts $T$ and $RH$ profiles for the 5% mass-loading case, although the differences between the
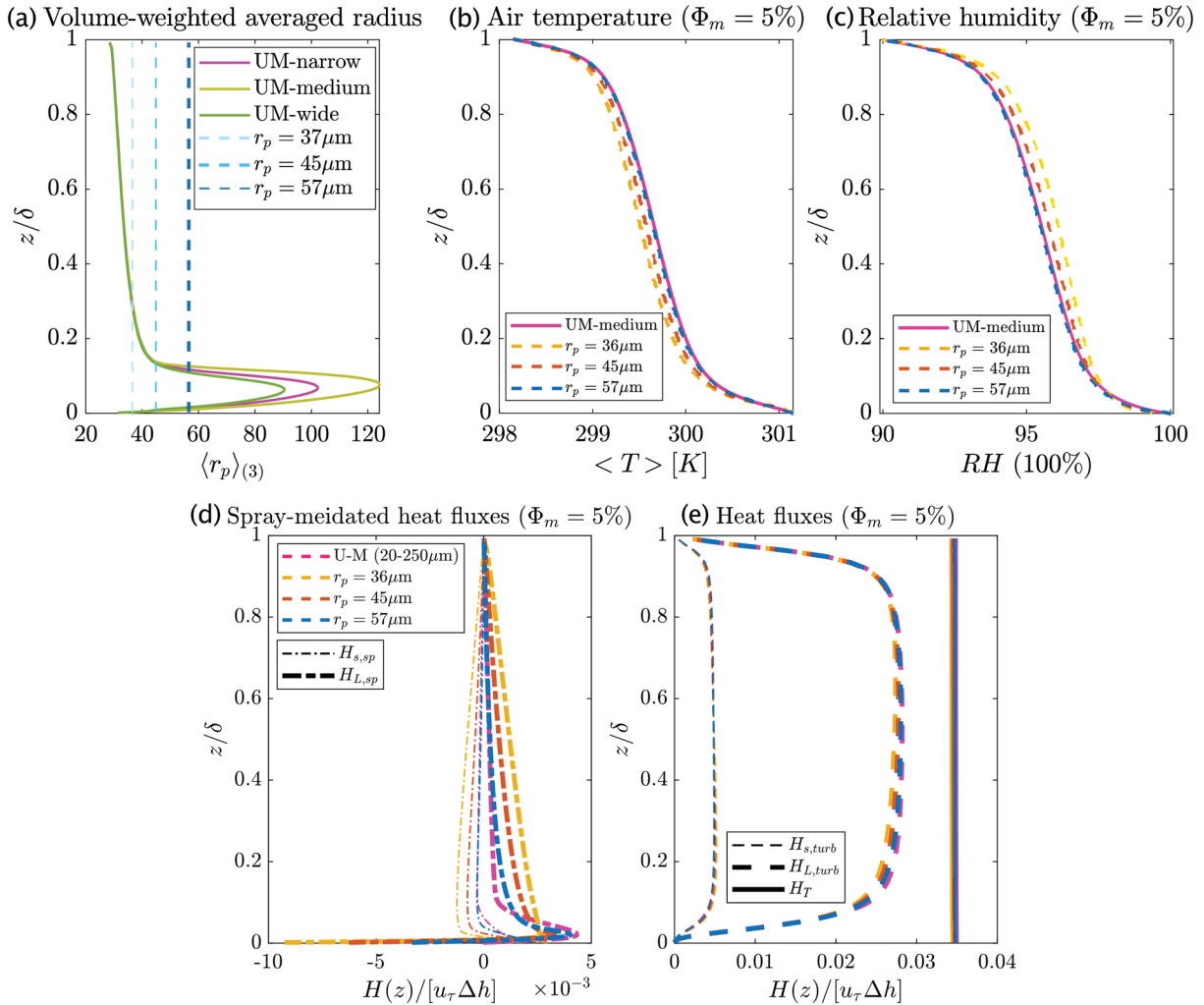
**Figure 8.** (a) The local volume-weighted mean radius as a function of height for three size ranges of the U-M DSD (solid lines), along with the three representative sizes for the whole distribution (dashed lines); (b) air temperature ($T$); (c) relative humidity ($RH$); (d) sensible and latent spray-mediated heat fluxes; and (e) turbulent and total heat flux for the three representative cases and the "UM-medium" case.

various radii are somewhat small. The predictions of $T$ and $RH$ are in contrast with what panels (b) and (c) in Figure 8 show, where the volume-weighted average of droplets radius in the upper domain is much less than $\langle r_p \rangle_{(3)}$ but closer to $\langle r_p \rangle_{(1)}$.

Focusing on the heat flux components, it is seen that the sensible spray-mediated (plotted in panel (d)) and turbulent heat fluxes (plotted in panel (e)) can be again generally predicted by a representative monodispersed DSD equal to the volume-weighted $\langle r_p \rangle_{(3)}$, although error occurs at the lower boundary. For example, panel (d) shows that $\langle r_p \rangle_{(3)}$ better predicts $H_{s,sp}$ compared to the latent component, although the volume-weighted $\langle r_p \rangle_{(3)}$ gives the closest prediction to the latent spray flux $H_{L,sp}$. Being less sensitive to the droplet size (heavy-size tail in particular), panel (e) shows that it may be possible to use $\langle r_p \rangle_{(3)}$ for predicting turbulent and total heat flux as an approximation to the full polydispersed DSD.

We also notice, comparing between the sensible and latent spray-mediated heat flux, that the volume-weighted representative size $\langle r_p \rangle_{(3)}$ better predicts the sensible heat fluxes. This effect can be explained as a combination of several factors. First, droplet size drastically decreases with the increasing domain height as seen in Figure 8a: only small droplets that are transported to the upper domain. That being said, the temperature response for these droplets is fast enough to reach the equilibrium temperature of
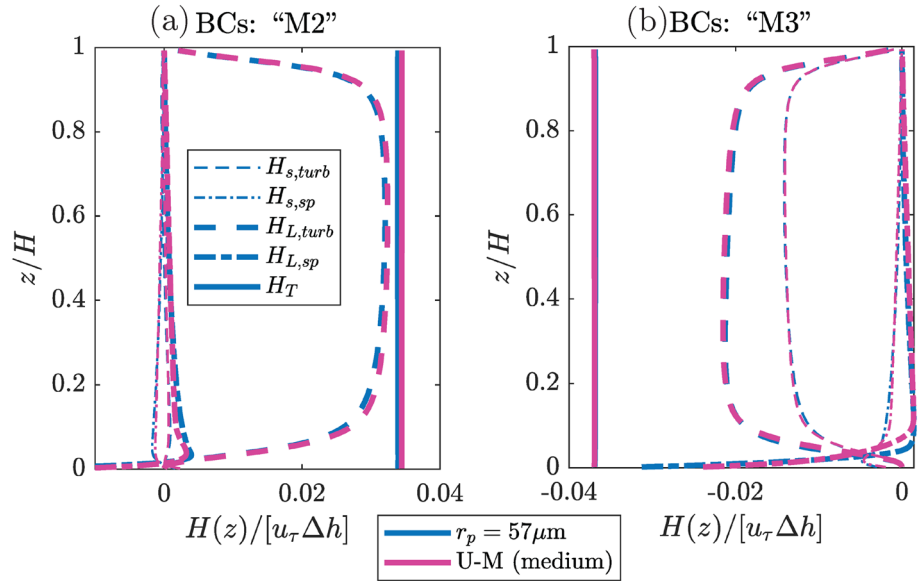
**Figure 9.** Comparisons of heat fluxes between the polydispersed cases and cases with the volume-weighted representative size ($r_p$=57 μm) for different boundary conditions listed in Table 2: (a) bottom and top boundaries have the same temperature ("M2"); and (b) inverse temperature difference ("M3").

evaporation, which is near the wet-bulb temperature (cf. Andreas, 1990). Also, the wet-bulb temperature is essentially the lowest droplet temperature which droplets can reach due to evaporation regardless of droplet size (Andreas, 1990), which indicates a similar influence from droplets smaller than a certain size on sensible spray-mediated flux.

As a final sensitivity and consistency check, we examine the different boundary conditions listed in Table 2 to compare the zero temperature difference (denoted as "M2") and the inverse temperature difference (denoted as "M3") to the benchmark boundary conditions. As one can see in Figure 9, under different boundary conditions, the volume-weighted representative size $\langle r_p \rangle_{(3)}$ again captures well the heat flux components across the domain, especially above the so-called spray layer ($\delta_{inj}$). Therefore, the volume-weighted average droplet size of a DSD is observed to be a robust approximation for the total heat flux of a polydisperse mixture.

## 4. Conclusions

In this paper, we investigate the effects of spray and in particular the influence of a polydisperse DSD on spray-mediate fluxes. Using a DNS framework similar to previous work (Peng & Richter, 2017, 2019), we critically examine common assumptions made in bulk models when combining the influence of spray droplets of varying radii. First, with idealized bidispersed experiments, we test the influences of droplet size combinations on the statistics of droplet temperature and radius change. We find that droplets with a ratio of residence time to thermal response time of $\tilde{t}_L \approx \mathcal{O}(1)$ are most susceptible to be indirectly influenced by other droplet sizes.

The indirect interactions between droplet sizes indicate that assuming independent contributions from different spray size classes may introduce errors in bulk and Lagrangian spray models (e.g., Andreas et al., 2015; Fairall et al., 1994; Mueller & Veron, 2014a, 2014b). When multiple sizes are present, we find a potential overestimate of bulk model predictions which is caused by overcounting the contribution of small droplets. We, therefore, put forward a correction by filtering out the contribution from droplets with $\tilde{t}_L > \mathcal{O}(1)$. This in turn successfully improves the accuracy of bulk estimates of the total heat flux.

For the spray-mediated heat fluxes, we further evaluate a bulk model that is related to spray sensible and latent heat exchange rate and inspired by Fairall et al. (1994, 2014b), as an extension of the monodispersed DSDs examined in Peng and Richter (2019). We find that the bulk estimates have additional difficulty

predicting the spray-mediated heat flux when considering the polydispersity of DSDs. While the bulk estimates generally capture the total spray-mediated heat flux, it struggles to predict the sensible components and all fluxes associated with the spray that has a time scale ratio $\tilde{t}_L = t_L/\tau_T \approx \mathcal{O}(1)$—the size range that is most susceptible to the influences from other sizes.

In an effort to test whether a polydisperse DSD can be approximated by a single representative droplet size, we evaluate three different DSD moments and their corresponding representative sizes. We find that the volume-weighted mean size predicts the modified air temperature and humidity fields well and quantitatively captures the vertical profiles of heat fluxes. As noted in Andreas et al. (2008,2015), this single droplet representation helps simplify and accelerate the computation of spray-mediated heat and moisture fluxes.

## Data Availability Statement

Supporting data and postprocessing scripts can be downloaded at CurateND hosted at the University of Notre Dame (https://curate.nd.edu/show/ff365428s00).

## References

Andreas, E. L. (1989). Thermal and size evolution of sea spray droplets, *CRREL Report 89-11* (pp. 1–38). Hanover, NH: US Army Corps of Eng., Cold Reg. Res. Eng. Lab.

Andreas, E. L. (1990). Time constants for the evolution of sea spray droplets. *Tellus B*, *42*(5), 481–497. https://doi.org/10.1034/j.1600-0889.1990.t01-3-00007.x

Andreas, E. L. (1992). Sea spray and the turbulent air-sea heat fluxes. *Journal of Geophysical Research*, *99*(C7), 14,345. https://doi.org/10.1029/92JC00876

Andreas, E. L. (1998). A new sea spray generation function for wind speeds up to 32 m s$^{-1}$. *Journal of Physical Oceanography*, *28*(11), 2175–2184.

Andreas, E. L. (2005). Approximation formulas for the microphysical properties of saline droplets. *Atmospheric Research*, *75*(4), 323–345. https://doi.org/10.1016/j.atmosres.2005.02.001

Andreas, E. L., Edson, J. B., Monahan, E. C., Rouault, M. P., & Smith, S. D. (1995). The spray contribution to net evaporation from the sea: A review of recent progress. *Boundary-Layer Meteorology*, *72*(1-2), 3–52. https://doi.org/10.1007/BF00712389

Andreas, E. L., & Emanuel, K. A. (2001). Effects of sea spray on tropical cyclone intensity. *Journal of the Atmospheric Sciences*, *58*, 3741–3751. https://doi.org/10.1175/1520-0469(2001)058<3741:EOSSOT>2.0.CO;2

Andreas, E. L., Mahrt, L., & Vickers, D. (2015). An improved bulk air-sea surface flux algorithm, including spray-mediated transfer. *Quarterly Journal of the Royal Meteorological Society*, *141*(687), 642–654. https://doi.org/10.1002/qj.2424

Andreas, E. L., Persson, P. O. G., & Hare, J. E. (2008). A bulk turbulent air-sea flux algorithm for high-wind, spray conditions. *Journal of Physical Oceanography*, *38*, 1581–1596. https://doi.org/10.1175/2007JPO3813.1

Andreas, E. L., Vlahos, P., & Monahan, E. C. (2016). The potential role of sea spray droplets in facilitating air-sea gas transfer. *IOP Conference Series: Earth and Environmental Science*, *35*, 012003. https://doi.org/10.1088/1755-1315/35/1/012003

Anguelova, M. D., & Bettenhausen, M. H. (2019). Whitecap fraction from satellite measurements: Algorithm description. *Journal of Geophysical Research: Oceans*, *124*, 1827–1857. https://doi.org/10.1029/2018JC014630

Bell, M. M., Montgomery, M. T., & Emanuel, K. A. (2012). Air-sea enthalpy and momentum exchange at major hurricane wind speeds observed during CBLAST. *Journal of the Atmospheric Sciences*, *69*(11), 3197–3222. https://doi.org/10.1175/JAS-D-11-0276.1

Brumer, S. E., Zappa, C. J., Brooks, I. M., Tamura, H., Brown, S. M., Blomquist, B. W., et al. (2017). Whitecap coverage dependence on wind and wave statistics as observed during SO GasEx and HiWinGS. *Journal of Physical Oceanography*, *47*(9), 2211–2235.

de Leeuw, G., Andreas, E. L., Anguelova, M. D., Fairall, C. W., Ernie, R., O'Dowd, C., et al. (2011). Production flux of sea-spray aerosol. *Reviews of Geophysics*, *49*, RG2001. https://doi.org/10.1029/2010RG000349

Druzhinin, O. A., Troitskaya, Y. I., & Zilitinkevich, S. S. (2017). The study of droplet-laden turbulent airflow over waved water surface by direct numerical simulation. *Journal of Geophysical Research: Oceans*, *122*, 1789–1807. https://doi.org/10.1002/2016JC012134

Druzhinin, O. A., Troitskaya, Y. I., & Zilitinkevich, S. S. (2018). The study of momentum, mass, and heat transfer in a droplet-laden turbulent airflow over a waved water surface by direct numerical simulation. *Journal of Geophysical Research: Oceans*, *123*, 8346–8365. https://doi.org/10.1029/2018JC014346

Edson, J. B., Anquetin, S., Mestayer, P. G., & Sini, J. F. (1996). Spray droplet modeling 2. An interactive Eulerian-Lagrangian model of evaporating spray droplets. *Journal of Geophysical Research*, *101*(C1), 1279–1293. https://doi.org/10.1029/95JC03280

Emanuel, K. A. (1986). An air-sea interaction theory for tropical cyclones. Part I: Steady-state maintenance. *Journal of the Atmospheric Sciences*, *43*(6), 585–605.

Emanuel, K. A. (2003). A similarity hypothesis for air-sea exchange at extreme wind speeds. *Journal of the Atmospheric Sciences*, *60*(11), 1420–1428. https://doi.org/10.1175/1520-0469(2003)060<1420:ASHFAE>2.0.CO;2

Fairall, C. W., Bradley, E. F., Hare, J. E., Grachev, A. A., & Edson, J. B. (2003). Bulk parameterization of air-sea fluxes: Updates andverification for the COARE algorithm. *Journal of Climate*, *16*(4), 571–591. https://doi.org/10.1175/1520-0442(2003)016<0571:BPOASF>2.0.CO;2

Fairall, C. W., Kepert, J. D., & Holland, G. J. (1994). The effect of sea spray on surface energy transports over the ocean. *The Global Atmosphere and Ocean System*, *2*, 121–142.

Gall, J. S., Frank, W. M., & Kwon, Y. (2008). Effects of sea spray on tropical cyclones simulated under idealized conditions. *Monthly Weather Review*, *136*(5), 1686–1705. https://doi.org/10.1175/2007mwr2183.1

Garg, N., Ng, E. Y. K., & Narasimalu, S. (2018). The effects of sea spray and atmosphere-wave coupling on air-sea exchange during a tropical cyclone. *Atmospheric Chemistry and Physics*, *18*(8), 6001–6021. https://doi.org/10.5194/acp-18-6001-2018

Gonçalves, I. A., & Innocentini, V. (2018). Analytical quantification of carbon dioxide exchange mediated by spume droplets. *Boundary-Layer Meteorology*, *169*(2), 327–345. https://doi.org/10.1007/s10546-018-0369-z

Helgans, B., & Richter, D. H. (2016). Turbulent latent and sensible heat flux in the presence of evaporative droplets. *International Journal of Multiphase Flow*, *78*, 1–11. https://doi.org/10.1016/j.ijmultiphaseflow.2015.09.010

Monahan, E. C., Staniec, A., & Vlahos, P. (2017). Spume drops: Their potential role in air-sea gas exchange. *Journal of Geophysical Research: Oceans*, *112*, 9500–9517. https://doi.org/10.1002/2017JC013293

Mueller, J. A., & Veron, F. (2010). A Lagrangian stochastic model for sea-spray evaporation in the atmospheric marine boundary layer. *Boundary-Layer Meteorology*, *137*(1), 135–152. https://doi.org/10.1007/s10546-010-9520-1

Mueller, J. A., & Veron, F. (2014a). Impact of sea spray on air-sea fluxes. Part II: Feedback effects. *Journal of Physical Oceanography*, *44*, 2835–2853. https://doi.org/10.1175/JPO-D-13-0246.1

Mueller, J. A., & Veron, F. (2014b). Impact of sea spray on air-sea fluxes. Part I: Results from stochastic simulations of sea spray drops over the ocean. *Journal of Physical Oceanography*, *44*, 2835–2853. https://doi.org/10.1175/JPO-D-13-0246.1

Ortiz-Suslow, D. G., Haus, B. K., Mehta, S., & Laxague, N. J. M. (2016). Sea spray generation in very high winds. *Journal of the Atmospheric Sciences*, *73*(10), 3975–3995. https://doi.org/10.1175/JAS-D-15-0249.1

Pan, M., Liu, C., Li, Q., Tang, S., Shen, L., & Dong, Y. (2019). Impact of spray droplets on momentum and heat transport in a turbulent marine atmospheric boundary layer. *Theoretical and Applied Mechanics Letters*, *9*(2), 71–78. https://doi.org/10.1016/j.taml.2019.02.002

Peng, T., & Richter, D. H. (2017). Influence of evaporating droplets in the turbulent marine atmospheric boundary layer. *Boundary-Layer Meteorology*, *165*(3), 497–518. https://doi.org/10.1007/s10546-017-0285-7

Peng, T., & Richter, D. H. (2019). Sea spray and its feedback effects: Assessing bulk algorithms of air-sea heat fluxes via direct numerical simulations. *Journal of Physical Oceanography*, *49*(6), 1403–1421. https://doi.org/10.1175/jpo-d-18-0193.1

Pruppacher, H. R., & Klett, J. D. (1996). *Microphysics of clouds and precipitation*: Springer Netherlands.

Ranz, W. E., & Marshall, W. R. (1952). Evaporation from drops: Part 1 and 2. *Chemical Engineering Progress*, *48*(3), 141–147, 173–180.

Rastigejev, Y., & Suslov, S. A. (2016). Two-temperature nonequilibrium model of a marine boundary layer laden with evaporating ocean spray under high-wind conditions. *Journal of Physical Oceanography*, *46*(10), 3083–3102. https://doi.org/10.1175/JPO-D-16-0039.1

Rastigejev, Y., & Suslov, S. A. (2019). Effect of evaporating sea spray on heat fluxes in a marine atmospheric boundary layer. *Journal of Physical Oceanography*, *49*, 1927–1948. https://doi.org/10.1175/jpo-d-18-0240.1

Richter, D. H., Dempsey, A. E., & Sullivan, P. P. (2019). Turbulent transport of spray droplets in the vicinity of moving surface waves. *Journal of Physical Oceanography*, *49*(7), 1789–1807. https://doi.org/10.1175/jpo-d-19-0003.1

Richter, D. H., Garcia, O., & Astephen, C. (2016). Particle stresses in dilute, polydisperse, two-way coupled turbulent flows. *Physical Review E*, *93*(1), 1–8. https://doi.org/10.1103/PhysRevE.93.013111

Richter, D. H., & Stern, D. P. (2014). Evidence of spray-mediated air-sea enthalpy flux within tropical cyclones. *Geophysical Research Letters*, *41*, 2997–3003. https://doi.org/10.1002/2014GL059746

Richter, D. H., & Sullivan, P. P. (2014). The sea spray contribution to sensible heat flux. *Journal of the Atmospheric Sciences*, *71*(2), 640–654. https://doi.org/10.1175/JAS-D-13-0204.1

Romero, L., Lenain, L., & Melville, W. K. (2017). Observations of surface wave-current interaction. *Journal of Physical Oceanography*, *47*(3), 615–632. https://doi.org/10.1175/jpo-d-16-0108.1

Salisbury, D. J., Anguelova, M. D., & Brooks, I. M. (2013). On the variability of whitecap fraction using satellite-based observations. *Journal of Geophysical Research: Oceans*, *118*, 6201–6222. https://doi.org/10.1002/2013JC008797

Schade, L. R., & Emanuel, K. A. (1999). The ocean's effect on the intensity of tropical cyclones: Results from a simple coupled atmosphere-ocean model. *Journal of the Atmospheric Sciences*, *56*(4), 642–651. https://doi.org/10.1175/1520-0469(1999)056<0642:TOSEOT>2.0.CO;2

Tang, S., Yang, Z., Liu, C., Dong, Y. H., & Shen, L. (2017). Numerical study on the generation and transport of spume droplets in wind over breaking waves. *Atmosphere*, *8*(12), 1–22. https://doi.org/10.3390/atmos8120248

Troitskaya, Y., Druzhinin, O., Kozlov, D., & Zilitinkevich, S. (2018). The bag breakup spume droplet generation mechanism at high winds. Part II: Contribution to momentum and enthalpy transfer. *Journal of Physical Oceanography*, *48*(9), 2189–2207. https://doi.org/10.1175/JPO-D-17-0105.1

Troitskaya, Y., Ezhova, E., Soustova, I., & Zilitinkevich, S. (2016). On the effect of sea spray on the aerodynamic surface drag under severe winds. *Ocean Dynamics*, *66*(5), 659–669.

Troitskaya, Y., Kandaurov, A., Ermakova, O., Kozlov, D., Sergeev, D., & Zilitinkevich, S. (2018). The bag breakup spume droplet generation mechanism at high winds. Part I: Spray generation function. *Journal of Physical Oceanography*, *48*(9), 2167–2188. https://doi.org/10.1175/JPO-D-17-0104.1

Van Eijk, A. M. J., Tranchant, B. S., & Mestayer, P. G. (2001). SeaCluse: Numerical simulation of evaporating sea spray droplets. *Journal of Geophysical Research*, *106*(C2), 2573–2588. https://doi.org/10.1029/2000JC000377

Veron, F. (2015). Ocean spray. *Annual Review of Fluid Mechanics*, *47*(1), 507–538. https://doi.org/10.1146/annurev-fluid-010814-014651

Veron, F., Hopkins, C., Harrison, E. L., & Mueller, J. A. (2012). Sea spray spume droplet production in high wind speeds. *Geophysical Research Letters*, *39*(16), 1–5. https://doi.org/10.1029/2012GL052603

Zeng, X., Zhao, M., & Dickinson, R. E. (1998). Intercomparison of bulk aerodynamic algorithms for the computation of sea surface fluxes using TOGA COARE and TAO data. *Journal of Climate*, *11*(10), 2628–2644. https://doi.org/10.1175/1520-0442(1998)011 <2628:IOBAAF>2.0.CO;2